



Electronic modulation with Pt-incorporated NiFe layered double hydroxide for ultrastable overall water splitting at 1000 mA cm⁻²

Xuedong He^{a,1}, Xiang Han^{a,1}, Xueyan Zhou^a, Jiadong Chen^a, Juan Wang^{a,*}, Yan Chen^a, Lianghao Yu^a, Nan Zhang^b, Jun Li^a, Shun Wang^{a,*}, Huile Jin^{a,c,**}

^a Wenzhou Key Lab of Advanced Energy Storage and Conversion, Zhejiang Province Key Lab of Leather Engineering, College of Chemistry and Materials Engineering, Wenzhou University, Wenzhou, Zhejiang 325035, China

^b Key Laboratory of Synthetic and Biological Colloids, Ministry of Education, School of Chemical and Material Engineering, Jiangnan University, Wuxi, Jiangsu 214122, China

^c Zhejiang Engineering Research Center for Electrochemical Energy Materials and Devices, Institute of New Materials and Industrial Technologies, Wenzhou University, Wenzhou, Zhejiang 325035, China

ARTICLE INFO

Keywords:

Water splitting
Oxygen evolution reaction
Hydrogen evolution reaction
NiFe layer double hydroxide

ABSTRACT

Achieving large current density is crucial to the practical application of large-scale hydrogen production by water splitting, but it is hindered by sluggish and unstable catalysts. Herein, a Pt-induced NiFe layered double hydroxide (Pt-NiFe LDH) nanosheet is synthesized for hydrogen evolution reaction (HER) and oxygen evolution reaction (OER). It affords 10 mA cm⁻² at overpotentials of only 198 mV and 36 mV for OER and HER, respectively. Impressively, an alkali-electrolyzer (Pt-NiFe LDH || Pt-NiFe LDH) exhibits a stable cell voltage of 1.887 V to deliver a current density of 1000 mA cm⁻² over 3000 h. The introduction of Pt modulates the electronic structure on the surface of NiFe LDH by charging redistribution at the interface and decreasing the Gibbs free energy change (ΔG) for the potential determining step (from *O to *OOH) during OER. This work provides a facile strategy for developing catalysts for large current density water splitting.

1. Introduction

Hydrogen is considered as one of the most promising energy carriers to replace traditional fossil fuels due to its energy-dense and carbon-neutral.[1,2] However, cracking or reforming fossil fuels are still majorly cost-effective pathways for industrial hydrogen production.[3] Electrochemical water splitting is regarded as an efficient and clean means for the production of hydrogen, which does not require further purification, among which electrolysis in alkaline has shown critical advantages in cost, stability, and industrialization.[4] The efficiency of water electrolysis in alkaline is still limited by the sluggish kinetic associated with driving the hydrogen evolution reaction (HER) and oxygen evolution reaction (OER), especially at large current density.[5] At present, novel-metal-based materials (Pt for HER, IrO₂, and RuO₂ for OER) are state-of-the-art electrocatalysts for water splitting.[6,7] However, high costs and poor stability limit their large-scale utilization.

[8–11] Therefore, it is urgent to design and develop highly stable and efficient catalysts for electrocatalytic applications.

It is desirable to develop electrocatalysts for high current density water splitting by overcoming a two-pronged challenge, reaction kinetics, and mass transport.[12,13] Transition metal (oxy)hydroxide exhibits impressive OER reaction kinetics, such as layered double hydroxide (LDH) based on Fe, Ni, and Co-based materials.[14–18] However, the weaker adsorption of hydrogen (H_{ad}) results in a large energy barrier for HER, leading to sluggish kinetics of the water splitting process.[19–22] Moreover, to achieve the practical applications of electrocatalytic water splitting, especially at a large current density (> 500 mA cm⁻²), it is particularly important to accelerate the kinetics on the catalyst surface and expand the contact efficiency between the catalyst and the electrolyte.[23,24] Therefore, emerging regulation strategies, including morphology control,[25,26] defects engineering,[27] and charge transfer[28,29] are used to solve the above obstacles. However,

* Corresponding authors.

** Corresponding author at: Wenzhou Key Lab of Advanced Energy Storage and Conversion, Zhejiang Province Key Lab of Leather Engineering, College of Chemistry and Materials Engineering, Wenzhou University, Wenzhou, Zhejiang 325035, China.

E-mail addresses: juanwang@wzu.edu.cn (J. Wang), shunwang@wzu.edu.cn (S. Wang), huilejin@wzu.edu.cn (H. Jin).

¹ Xuedong He and Xiang Han contribute equally to this work.

the sophisticated multistep processes and rigorous experimental conditions severely limit their prospects for large-scale applications. Compared to hydrothermal methods, corrosion engineering, and atomic layer deposition (ALD), [30] electrodeposition is an economical, high-efficiency, and binder-free method for practical application. Ni foam (NF), as a substrate for fabricating self-supporting catalysts, can effectively accelerate oxygen and electrolyte transport due to its three dimensional (3D), cross-linked, porous structure. In addition, metal clusters have been widely reported as efficient catalysts with unusual selectivity and activity for different catalytic reaction due to their unique physical and chemical features. [31,32] Therefore, the combination of 3D self-supporting structures and clusters is expected to achieve the goal of high current density water splitting.

Herein, we demonstrate Pt clusters induced uniform interconnected NiFe layered double hydroxide (Pt-NiFe LDH) nanosheets by simple electrodeposition for efficient water splitting. The Pt-NiFe LDH exhibits overpotentials of 198 mV and 226 mV at 10 mA cm⁻² and 100 mA cm⁻² for the OER process in 1.0 M KOH. Additionally, as-synthesized Pt-NiFe LDH achieves a current density of 10 mA cm⁻² at an overpotential of 36 mV and has a high mass activity and turnover frequency (TOF) for HER. Inspired by the superior OER and HER performances, Pt-NiFe LDH was used as a bifunctional electrocatalyst for water splitting. Surprisingly, a current density of up to 1000 mA cm⁻² can be achieved with a voltage of only 1.897 V, and it can be operated continuously for more than 3000 h, significantly superior to most reported catalysts (Table S1–3). Density functional theory (DFT) calculations demonstrate that the Pt-NiFe LDH interface could lower the reaction barriers of OER. This work represents a facile strategy for constructing promising candidates for efficient and ultra-stable electrocatalysts toward water splitting.

2. Experimental section

2.1. materials

Nickel foam (NF) was purchased from Kejing Co., Ltd. (Shenzhen, China). Iron(III) nitrate nonahydrate (Fe(NO₃)₃·9 H₂O, 99%), Hydrogen hexachloroplatinate (H₂PtCl₆·(H₂O)₆) were purchased from Aladdin Co., Ltd. (Shanghai, China), hydrochloric acid (HCl) was purchased from Zhongxing Co., Ltd. (Lanxi, China). Pt/C (20 wt% Pt on Vulcan black) and IrO₂ were purchased from Shanghai Hesen Electric Co., Ltd. All reagents in this work were used as received without further purification. Ultrapure Milli-Q water was used in all experiments.

2.2. Synthesis of Pt-NiFe LDH, NiFe LDH, Pt-Ni(OH)₂, and Ni(OH)₂

NF was immersed in 2 M HCl to remove the surface oxide layer, followed by immersion in ethanol and water for further cleaning. Electrodeposition was carried out in a three-electrode cell with NF, carbon rod, and saturated calomel electrode (SCE) as a working electrode, a counter electrode, and a reference electrode, respectively. In detail, the 45 mL electrolyte contains 1.939 g of Fe(NO₃)₃·9 H₂O. Constant potential electrodeposition was conducted at -1.2 V versus (vs.) SCE for 60 s. After electrodeposition treatment, as-fabricated catalysts were washed with deionized water several times, and dried in the oven at 80 °C (named NiFe LDH). Subsequently, 5 mg of H₂PtCl₆·(H₂O)₆ was added to 60 mL of KCl solution. The electrodeposition was implemented by triangular-wave voltage for 10 cycles with a range from 0 to -0.5 V (vs. SCE) at a scan rate of 100 mV s⁻¹. Finally, the catalysts were washed and dried in the oven (named Pt-NiFe LDH). NiFe LDH was prepared by using the same steps, except no electrodeposition in H₂PtCl₆·(H₂O)₆ solution. Pt-Ni(OH)₂ and Ni(OH)₂ were prepared in the electrolyte with Ni(NO₃)₂·6 H₂O and electrodeposition with H₂PtCl₆·(H₂O)₆ and without H₂PtCl₆·(H₂O)₆, respectively.

2.3. Characterization

Scanning electron microscopy (SEM) images were recorded on a Nova Nanosem 200 system operated at an acceleration voltage of 10 kV. Transmission electron microscopy (TEM) and Energy-dispersive X-ray spectroscopy (EDX) was performed on the JEOL-2100 instrument. X-ray photoelectron spectroscopy (XPS) dates were conducted on a spectrometer from Kratos Axis Ultra DLD, using Mono Al K α radiation at a power of 120 W (8 mA, 15 kV). X-ray diffraction (XRD) was measured on a Bruker D8 Advance diffractometer using Cu K α radiation (λ = 0.15406 nm), in which the data was collected in a range of 2θ = 10–80° with step size 0.02°. The concentration of catalysts was determined by the inductively coupled plasma atomic emission spectroscopy (ICP-AES) (PerkinElmer 8300). The optical photos and video of gas bubbles under electrolyte were recorded using an Olympus DSX1000 with a macro lens.

2.4. Electrochemical measurements

The electrochemical tests were carried out on an electrochemical workstation CHI 760E equipped with a current amplifier (CHI 680 C) at room temperature. A surface area of 1 cm² on each working electrode keeps exposed, with the rest of the electrode sealed with hot melt adhesives. A carbon rod as the counter electrode and a Hg/HgO electrode as the counter and reference electrode, respectively. The HER and OER activity were tested in a 1.0 M KOH solution. Cyclic voltammetry (CV) and linear sweep voltammetry (LSV) with a scan rate of 5 mV s⁻¹ (95% *iR* compensation). Electrochemical impedance spectroscopy (EIS) was performed with a frequency range from 100 kHz to 0.1 Hz. The electrochemical surface area (ECSA) was obtained by CVs at different scan rates from 20 to 120 mV s⁻¹. The TOF value can be calculated by the equation:

$$\text{TOF} = (jA)/(4Fn)$$

Where *j* is the current density at a constant overpotential, *A* is the area of the working electrode, *F* is Faraday's constant (96,485.3 C mol⁻¹) and *n* is the number of moles of the active materials. The energy of water splitting is calculated according to the formula:

$$W = UIt$$

Where *U* is the voltage of electrolyzer, *I* is the current, and *T* is time.

2.5. Theoretical calculations

The DFT + *U* calculations were conducted using the Vienna ab initio simulation package (VASP) [33,34] with the Projector Augmented Wave (PAW) [35,36] method. And the Perdew-Burke-Ernzerhof (PBE) function was employed to describe the exchange-correlation term with the on-site Coulomb repulsion *U* term. The van der Waals interaction was considered by DFT-D3 correction. According to the previous reports [37,38], the *U* values are set as 4.3 and 5.5 for Fe and Ni, respectively. The cutoff energy is fixed as 400 eV in all calculations. For geometry optimization, 10⁻⁵ eV and 0.02 eV Å⁻¹ are selected for convergence criteria of energy and force, respectively. The 2 × 2 × 1 and 5 × 5 × 1 Monkhoest-Pack k-point were employed in geometry optimization and electronic structure calculation. According to the in-situ Raman, NiOOH was detected during the OER. Therefore, the model of NiFe LDH was built on the NiOOH with partial Ni replaced by Fe atoms, forming NiFeOOH. And the Pt-NiFe LDH was modeled by placing Pt cluster on NiFeOOH. The adsorption energy of intermediates *X* on the slab was calculated by: $E_{\text{ads}} = E_{\text{X/slab}} - E_{\text{slab}} - E_{\text{X}}$. The Gibbs free energy was defined as $G = E_{\text{DFT}} + E_{\text{ZPE}} - TS_{\text{vib}}$, where E_{DFT} is the DFT-optimized total energy, E_{ZPE} is the zero-point energy, and TS_{vib} is obtained by the Harmonic-oscillator approximation and used for the vibrational entropy corrections. The free energy of gaseous O₂ is determined as: $G(\text{O}_2) = 2G(\text{H}_2\text{O}) - 2G(\text{H}_2)$

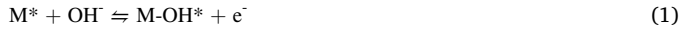
+ 4.92.

The ν -band center was calculated by the following formula:

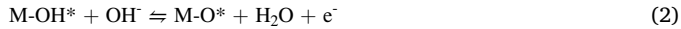
$$\varepsilon_d = \frac{\int_{-\infty}^{\infty} n_d(\varepsilon) \varepsilon d\varepsilon}{\int_{-\infty}^{\infty} n_d(\varepsilon) d\varepsilon}$$

Where ε is the energy referring to E-Fermi and $n_d(\varepsilon)$ is DOS projected onto ν -states.

The OER mechanism was described by the following four-electrons transfer process.



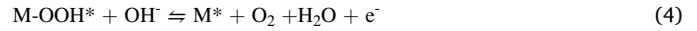
$$\Delta G_1 = G(M-OH^*) + eU - G(OH^-) - G(M^*)$$



$$\Delta G_2 = G(M-O^*) + G(H_2O) + eU - G(OH^-) - G(M-OH^*)$$



$$\Delta G_3 = G(M-OOH^*) + eU - G(OH^-) - G(M-O^*)$$



$$\Delta G_4 = G(M^*) + G(O_2) + G(H_2O) + eU - G(M-OOH^*) - G(OH^-)$$

3. Results and Discussion

3.1. Structural characterizations

As illustrated in Fig. 1a, Pt-NiFe LDH was synthesized on pretreated NF by facile electrodeposition. Briefly, constant potential electrodeposition was carried out in a solution containing ferric nitrate for a certain period to obtain self-supporting NiFe LDH. Subsequently, Pt nano-clusters were anchored on the surface of NiFe LDH by triangular-wave voltage. In addition, the contents of Pt for Pt-NiFe LDH are 7.3 wt% by ICP-AES analysis (Table S4). SEM images show that the Pt-NiFe LDH is distributed on the NF to form vertically 3D arrays (Fig. 1b and Fig. S1),

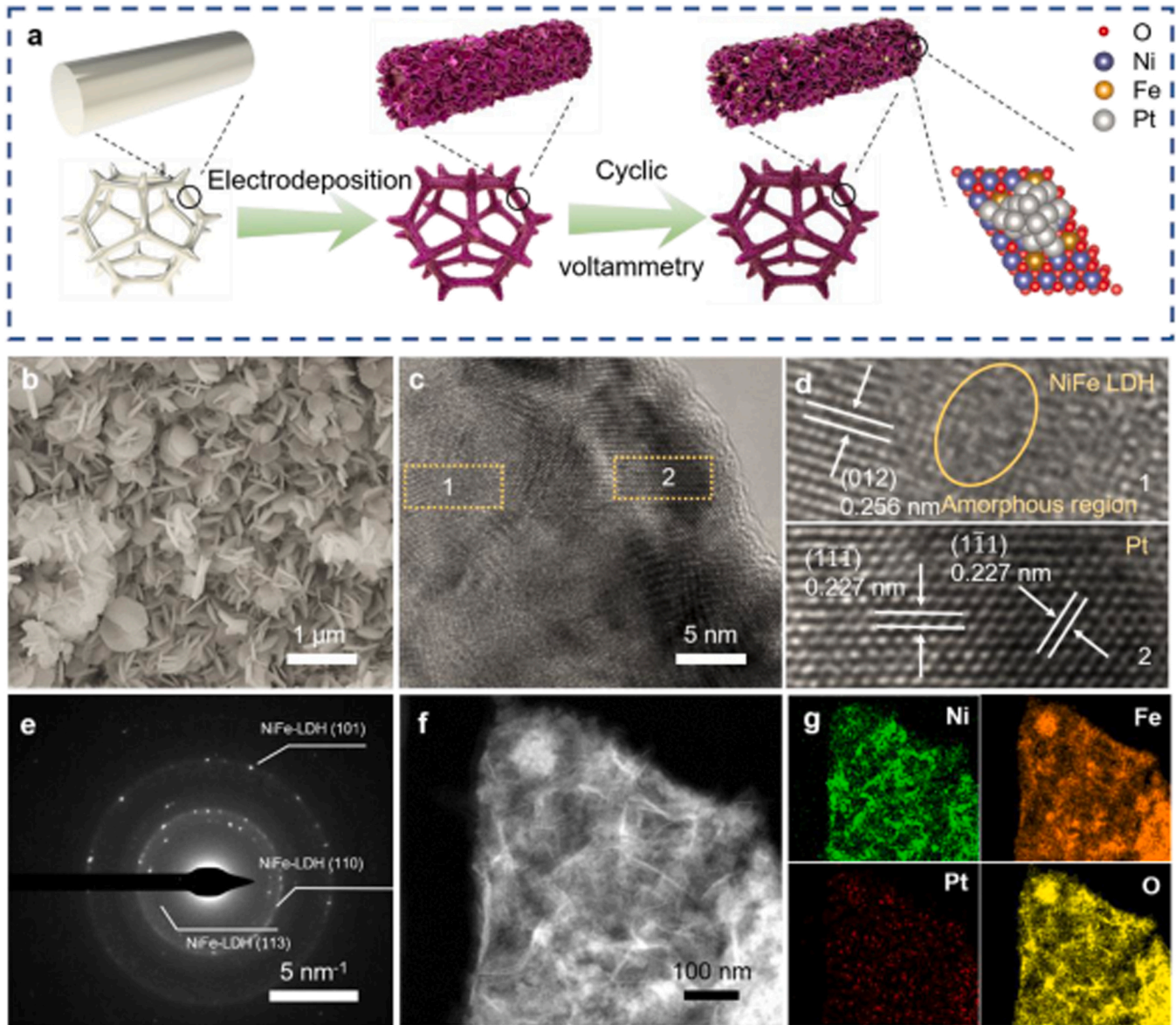


Fig. 1. (a) Schematic synthetic process for the Pt-NiFe LDH (Ni, Fe, O, Pt atoms are marked with purple, gold, red, and silver circles), (b) SEM image, (c, d) HRTEM images, and (e) SAED pattern, (f) HAADF-STEM, and corresponding (g) EDS elemental mappings of Pt-NiFe LDH.

which have a similar morphology as Pt-Ni(OH)₂ and NiFe LDH (Fig. S2 and S3). Additionally, energy-dispersive X-ray spectroscopy (EDS) was conducted, and the Fe, Ni, O, and Pt elements can be practically detected in all the positions. (Fig. S4). According to the TEM analysis, the average size of the Pt loaded on NiFe LDH is about 5.2 nm (Fig. S5). High-resolution TEM (HRTEM) images show that Pt-NiFe LDH exhibits distinct crystal stripes with plane spacing of 0.256 nm, which can be referred to the (012) plane of NiFe LDH phase (Fig. 1c, d). Notably, a distinct amorphous region can be observed in NiFe LDH, indicating the

presence of a large number of defect and unsaturated sites that can serve both as anchoring sites for stabilizing Pt nanoparticles and as active site to catalyzing OER/HER. [39,40] In addition, the crystal stripe spacings of 0.227 nm can be referred to the Pt {111} habit planes, which confirmed the formation of Pt nanoparticles. [41,42] The selected-area electron diffraction (SAED) pattern shows bright spots of NiFe LDH (Fig. 1e). Meanwhile, the high-angle annular dark-field scanning TEM (HAADF-STEM) image and EDS elemental mappings prove the homogeneous distribution of Ni, Fe, O, and Pt elements in the entire Pt-NiFe

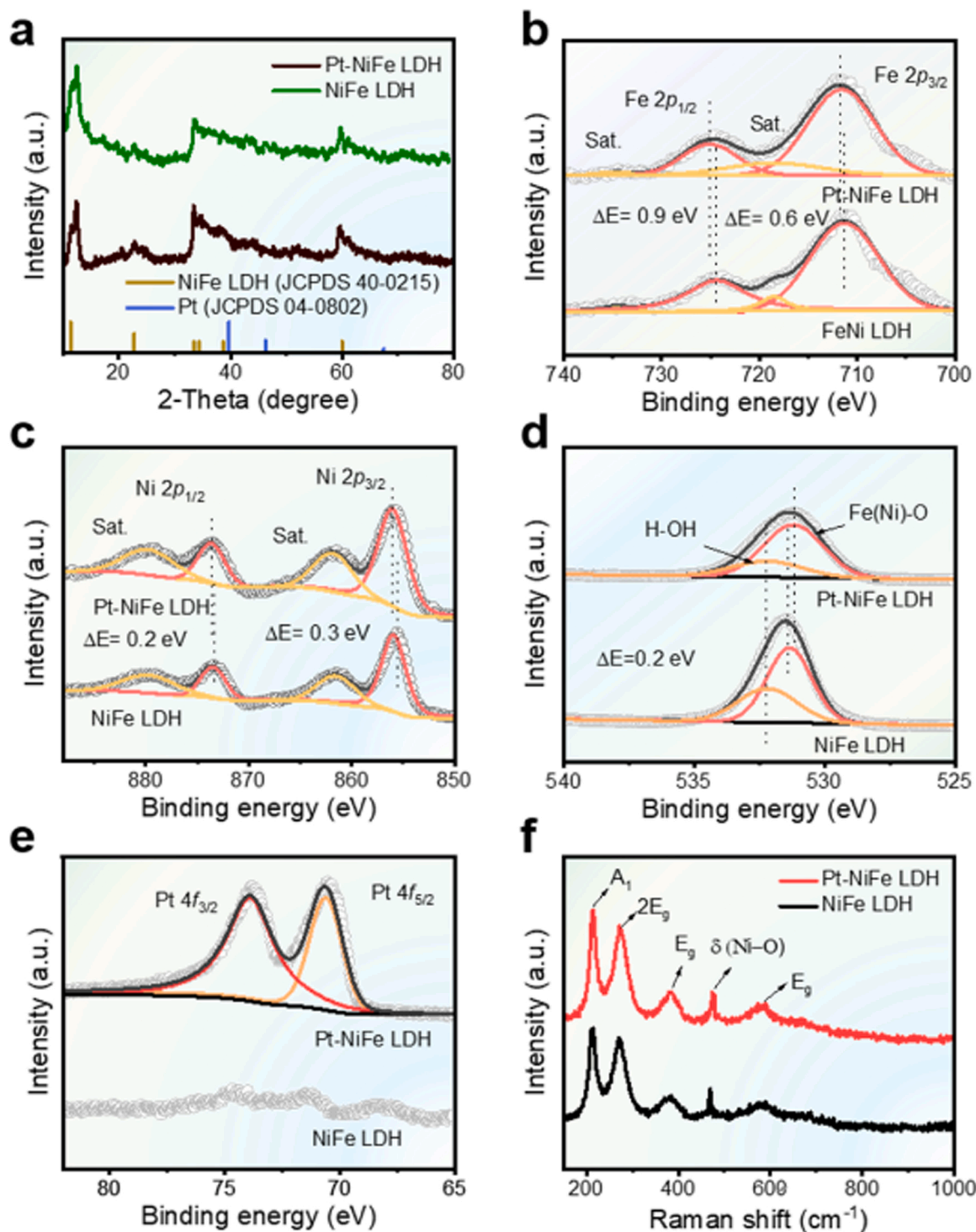


Fig. 2. (a) XRD pattern of NiFe LDH and Pt-NiFe LDH. (b) Fe 2p, (c) Ni 2p, (d) O 1 s, and (e) Pt 4 f XPS spectra of Pt-NiFe LDH and NiFe LDH. (f) Raman spectra of NiFe LDH and Pt-NiFe LDH.

LDH (Fig. 1f and g).

The Pt-NiFe LDH are stripped from NF and then X-ray diffraction (XRD) is measured immediately. As shown in Fig. 2a, the diffraction peaks centered at 12° , 23° , 33.4° , and 59.6° correspond to the (003), (006), (012), and (110) planes of NiFe LDH, respectively.[43] To determine the surface chemical state and electronic structure, an X-ray photoelectron spectroscopy (XPS) survey was recorded. According to the XPS spectra of Pt-NiFe LDH and NiFe LDH, Pt, Ni, Fe, O elements are proved in Pt-NiFe LDH (Fig. S6). Compare to NiFe LDH, the peaks of Fe $2p_{3/2}$ and Fe $2p_{1/2}$ of Pt-NiFe LDH show positive shifts of about 0.6 and 0.9 eV, respectively, implying the electronic coupling of Pt nanoclusters and NiFe LDH (Fig. 2b) [44–46], which is vital for changing the adsorption of intermediates during the OER process.[47,48] Fig. 2c shows the XPS spectra of Ni $2p$, whereas the binding energies (BEs) at

856.2 eV (Ni $2p_{3/2}$) and 873.8 eV (Ni $2p_{1/2}$) were attributed to the existence of Ni^{2+} . Significantly, the Ni $2p$ peaks of Pt-NiFe LDH exhibits a positive shift of approximately 0.2–0.3 eV compared to the peaks of the unmodified NiFe LDH. The O $1s$ XPS spectra of Pt-NiFe LDH and NiFe LDH were shown in Fig. 2d, the main broad peaks can be deconvoluted into two subpeaks with BEs of 531.2 and 532.3 eV, corresponding to the Fe(Ni)-O and H_2O , respectively.[45] Moreover, a negative shift is observed in O $1s$ XPS of Pt-NiFe LDH in comparison to NiFe LDH, suggesting the presence of intimate interaction between Pt atoms and NiFe LDH.[49,50] The Pt $4f$ XPS spectrum of Pt-NiFe LDH was deconvoluted into two components (Fig. 2e). The peaks at 74.2 and 71.4 eV were assigned to the $4f_{3/2}$ and $4f_{5/2}$ signals of metallic Pt, respectively, which indicates the presence of Pt.[51] The Pt-NiFe LDH was further studied by the Raman spectrum, the Raman peaks at 212, 271, 378, and

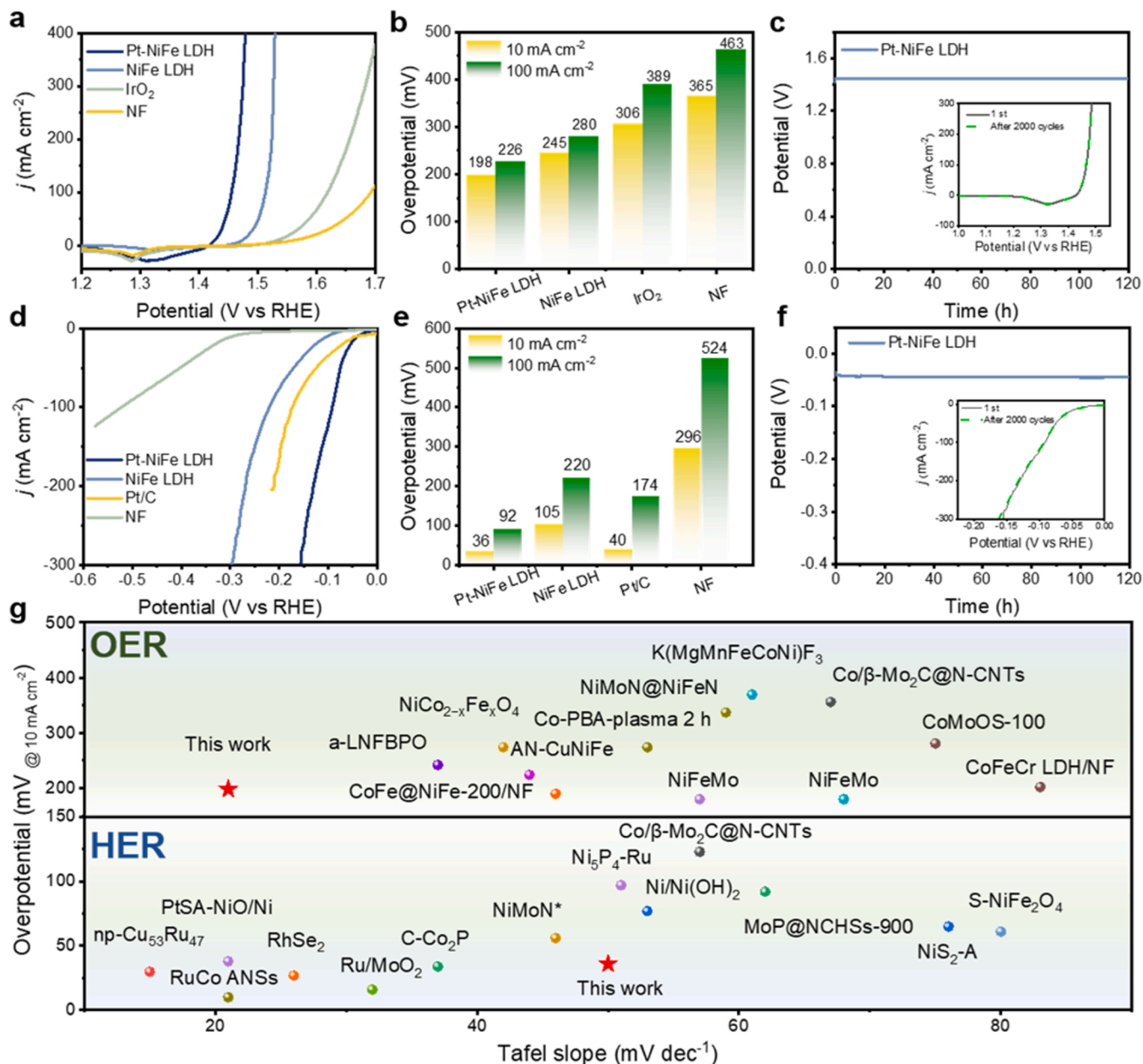


Fig. 3. (a) Polarization curves of OER, (b) the overpotentials at the current densities of 10 mA cm^{-2} and 100 mA cm^{-2} , and (c) the chronopotentiometry test of Pt-NiFe LDH under a current density of 10 mA cm^{-2} over 24 h (inset is LSV curves before and after 2000 cycles of CV). (d) Polarization curves of HER, (e) the overpotentials at the current densities of 10 mA cm^{-2} and 100 mA cm^{-2} , and (f) the chronopotentiometry test of Pt-NiFe LDH under a current density of 10 mA cm^{-2} over 24 h (inset is LSV curves before and after 2000 cycles of CV). (g) Comparison of the Tafel slope and the overpotential at 10 mA cm^{-2} for Pt-NiFe LDH with reported OER/HER electrocatalysts.

579 cm^{-1} are matched well with the A_1g , $2E_g$, and E_g stretching mode of Fe-O (Fig. 2f). [52] Meanwhile, the characteristic Raman peaks appeared at 473 cm^{-1} , which can be assigned to the vibrations of δ (Ni-O). [53].

3.2. Electrocatalytic OER/HER measurement

The electrocatalytic OER activity of Pt-NiFe LDH was evaluated in an oxygen-saturated 1.0 M KOH solution. For comparison, NiFe LDH, bare NF, and IrO_2 were measured under the same conditions. Notably, Pt-NiFe LDH exhibits the small OER overpotentials of 198 mV and 226 mV at 10 mA cm^{-2} and 100 mA cm^{-2} , much lower than those of NiFe LDH (245 mV and 280 mV), IrO_2 (306 mV and 389 mV), and NF (365 mV and 463 mV) (Fig. 3a and b). For comparison, Pt-NiCo LDH, Pt-Ni(OH)₂, CoNi LDH, and Ni(OH)₂ were tested under similar conditions. The Pt-NiCo LDH exhibits the best activity among them but is still far from Pt-NiFe LDH (Fig. S7). Tafel plots of various catalysts can be seen in Fig. S8a, where Pt-NiFe LDH exhibits a small Tafel slope of 21 mV dec^{-1} , which is lower than those of NiFe LDH (33 mV dec^{-1}), IrO_2 (46 mV dec^{-1}), and NF (103 mV dec^{-1}), respectively, suggesting its favorable reaction kinetics. To verify the above speculation, electrochemical impedance spectroscopy (EIS) tests were conducted (Fig. S8b), the charge-transfer resistance (R_{ct}) value of Pt-NiFe LDH is smaller than that of other catalysts for the OER process, which demonstrates faster charge-transfer kinetics. To study the origin of the enhancement of OER performance, electrochemical active surface area (ECSA) was calculated from the double layer capacitance (C_{dl}) in the non-Faradaic region. As displayed in Fig. S9, the C_{dl} value of Pt-NiFe LDH is 2.79 mF cm^{-2} , which is larger than those of NiFe LDH (1.56 mF cm^{-2}) and NF (0.91 mF cm^{-2}), implying more exposure of electrochemical active surface and hence higher OER performance. As shown in Fig. 3c, the durability of Pt-NiFe LDH was further investigated by chronopotentiometry method at 10 mA cm^{-2} for 120 h. Moreover, the linear sweep voltammetry (LSV) curve of Pt-NiFe LDH approximates the initial one after 2000 cyclic voltammetry (CV) (inset in Fig. 3c), further indicating that Pt-NiFe LDH possesses excellent cycling stability in alkaline solution.

The HER activity of catalysts was also investigated in a three-electrode system in 1.0 M KOH. The Pt-NiFe LDH exhibits the overpotential of 36 mV and 92 mV at 10 mA cm^{-2} and 100 mA cm^{-2} , significantly lower than those of NiFe LDH (105 mV and 220 mV), Pt/C (40 mV and 174 mV), and NF (296 mV and 524 mV) (Fig. 3d and e). Moreover, the Tafel slope of Pt-NiFe LDH is 50 mV dec^{-1} , better than those of NiFe LDH (80 mV dec^{-1}), Pt/C (125 mV dec^{-1}), and NF (119 mV dec^{-1}), indicating that Pt-NiFe LDH is a new class of highly promising HER catalysts (Fig. S10a). From Nyquist plots, Pt-NiFe LDH exhibits the smallest semicircle diameter, implying a faster charge transfer (Fig. S10b). Surprisingly, an impressive mass activity, 3472 $\text{A g}_{\text{Pt}}^{-1}$ of Pt-NiFe LDH was obtained at -0.1 V (Fig. S11), which is ~ 40 times higher than that of Pt/C (87 $\text{A g}_{\text{Pt}}^{-1}$). Furthermore, TOF is calculated to evaluate the intrinsic catalytic activity, where the calculated TOF of Pt-NiFe LDH is 6.78 s^{-1} , which is about 25-fold that of Pt/C (0.27 s^{-1}) at the overpotential of 100 mV (Fig. S12). In addition, Pt-NiFe LDH has impressive durability for the HER process (Fig. 3f). It is worth mentioning that the combined advantages of Pt-NiFe LDH, including low overpotential and Tafel slope, are superior to recently reported OER and HER catalysts (Fig. 3g and Table S1, S2).

Additionally, SEM, TEM and XPS analysis were performed to study the structure and surface chemical composition of Pt-NiFe LDH after the 2000 cycles of the CV test in OER and HER, respectively. There is little change in morphologies and structure of Pt-NiFe LDH after OER (Fig. S13, 14). Remarkably, the chemical state of Pt did not change significantly, but a positive shift is observed in Fe 2p and Ni 2p XPS spectra of Pt-NiFe LDH after the OER test, indicating the formation of a high valence state of Ni and Fe due to the oxidation of Pt-NiFe LDH (Fig. S15). The SEM result reveal that the morphology of Pt-NiFe LDH is retained well after the HER, further suggesting the good stability of Pt-NiFe LDH (Fig. S16).

3.3. Overall water splitting

Considering the excellent OER and HER performance of Pt-NiFe LDH in alkaline media, a two-electrode configuration electrolyzer for overall water splitting was assembled by using Pt-NiFe LDH as both anode and cathode (Fig. 4a). Based on the physics of boiling, when the radius of the gas bubble is smaller, the detachment frequency is higher. [54] Therefore, for the NF electrode, a much bigger bubble was observed (Fig. 4b). On contrary, a relatively small bubble is released from Pt-NiFe LDH during the OER test at the current 10 mA cm^{-2} (Fig. 4c). In addition, the video (Video S1–2) can further demonstrate the bubble changes after facile electrodeposition. According to the rough Cassie model, the desorption speed of the electrode on the Cassie surface is faster than that smooth surface. [23] The small stress induced by the small bubbles can effectively prevent the catalyst from falling off, thereby prolonging the service life of the catalyst. [55] To derive 10 mA cm^{-2} , only a cell voltage of 1.46 V was required for Pt-NiFe LDH || Pt-NiFe LDH (Fig. 4d), which is better than NiFe LDH || NiFe LDH (1.55 V), and Pt/C || IrO_2 (1.56 V). Pt-NiFe LDH || Pt-NiFe LDH presents a Faradaic efficiency close to 100% for both the HER and OER (Fig. S17). As shown in Fig. S18, Pt-NiFe LDH affords current densities of 1000 mA cm^{-2} at 1.887 V (85% iR correction). It is worth noting that the Pt-NiFe LDH displays impressive performance for overall water splitting with no sign of decay for over 3000 h when operated at constant current density of 1000 mA cm^{-2} (Fig. 4e). NiFe LDH || NiFe LDH also exhibits a remarkable stability, maintaining a relatively high performance at a current density of 1000 mA cm^{-2} for a prolonged period of 200 h (Fig. S19). Furthermore, Pt-NiFe LDH || Pt-NiFe LDH electrolyzer can be driven by 1.498 V solar cells (Fig. S20 and Video S3). Compared with the recently reported bifunctional water splitting electrocatalysts, the Pt-NiFe LDH ranks among the top promising candidates (Fig. 4f). According to the Nernst equation, the kinetics of HER and OER can be further boosted by increasing KOH concentration and the reaction temperature. Therefore, an electrolyzer with the operation of 6.0 M KOH and 333.15 K temperature was built in Fig. S21. Obviously, the electrolyzer voltage decreased with the increase in temperature (from 293.15 K to 333.15 K). Voltage decreases from 3.5 V to 2.8 V when the temperature increases from 293.15 K to 333.15 K. For a rough calculation, to prepare 1 kg hydrogen at the current density of 2000 mA cm^{-2} , Pt-NiFe LDH || Pt-NiFe LDH electrolyzer (92.3 kWh) can save 18.4 kWh electricity compared to the NF || NF electrolyzer. In addition, the smaller fluctuation of Pt-NiFe LDH || Pt-NiFe LDH electrolyzer voltage indicates its excellent activity and fast mass transfer (inset in Fig. S21).

Supplementary material related to this article can be found online at [doi:10.1016/j.apcatb.2023.122683](https://doi.org/10.1016/j.apcatb.2023.122683).

3.4. Mechanism investigation

To disclose the in-depth reason for the enhanced OER activity at the atomic level, in-situ Raman test was performed for Pt-NiFe LDH during OER process (Fig. 5a). When the applied potential was higher than 1.4 V vs. reversible hydrogen electrode (RHE), a pair of characteristic Raman peaks appear at 482 cm^{-1} and 555 cm^{-1} , which can be assigned to the e_g and A_1g mode of NiOOH. [56] When the applied potential decreases to 1.2 V vs. RHE, the peak of NiOOH disappeared. Based on the above results, DFT calculations were carried out to investigate the reason for the superior OER performances of Pt-NiFe LDH. From the charge density difference of Pt-NiFe LDH, obvious charge redistribution is observed at the interface (Fig. 5b). It could be seen that charge accumulates around the oxygen sites of NiFe LDH and is depleted around Pt, indicating electrons transfer from Pt to NiFe LDH. The charge contours at the interface between the NiFe and Pt were significantly dense compared with other areas, which can facilitate the adsorption of intermediates. In addition, the d -band center of Ni and Fe atoms gradually moves closer to the Fermi level after the introduction of Pt on NiFe LDH, suggesting that the Pt-NiFe LDH is more favourable for the adsorption of reactive

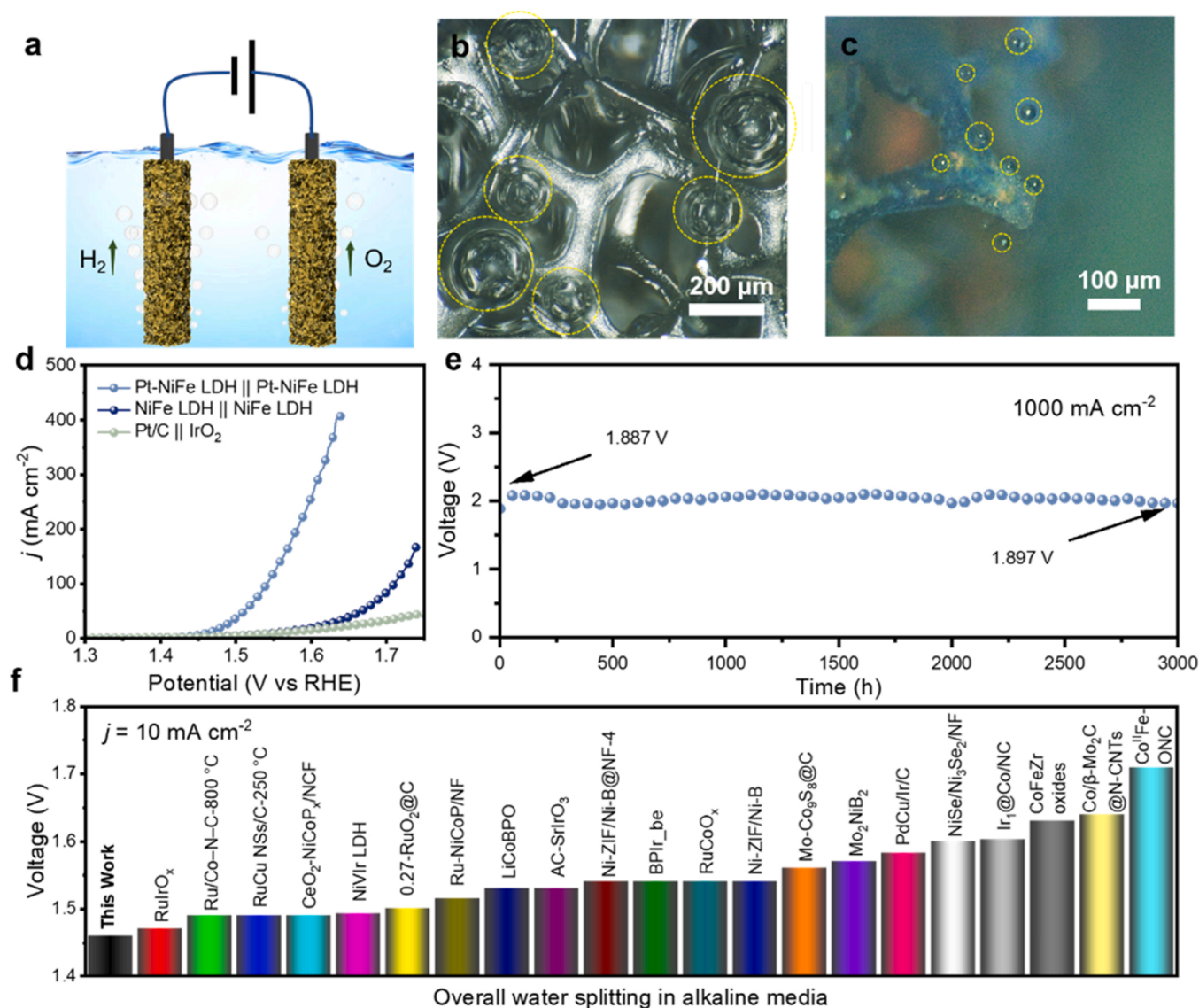


Fig. 4. (a) Schematic diagram of water splitting in a two-electrode system. Optical photos of O_2 bubbles attached to (b) NF and (c) Pt-NiFe LDH. (d) LSV curves by two-electrode configuration using different electrodes, (e) the chronopotentiometry test of Pt-NiFe LDH under a current density of 1000 mA cm $^{-2}$. (f) Comparison of the voltage at the current density of 10 mA cm $^{-2}$ for Pt-NiFe LDH with reported bifunctional electrocatalysts.

intermediates than NiFe LDH (Fig. 5c). [57] As depicted in Fig. 5d and e, the density of states (DOS) across the Fermi level of Pt-NiFe LDH is higher than that of NiFe LDH, which manifests that the introduction of Pt clusters increases the conductivity of NiFe LDH. The OER is generally considered to involve four proton-coupled electron transfer procedures, as described in Fig. 5f. The elementary steps in OER process over Pt-NiFe LDH and NiFe LDH were investigated in Fig. S22. NiFe at interface between Ni(Fe)OOH and Pt cluster as active sites to study the OER process. The Gibbs free energy diagrams of the OER at $U = 1.23$ V and $U = 0$ V are shown in Fig. 5g and h for Pt-NiFe LDH and NiFe LDH, respectively. The rate-determining step (RDS) during OER for these catalysts is $*O$ to $*OOH$, and the Gibbs free energy of RDS for Pt-NiFe LDH and NiFe LDH is 0.52 eV and 0.77 eV at $U = 1.229$ V, respectively. This indicates that the introduction of Pt on NiFe LDH reduces the energy barrier to boost activities. Thus, both experiment and theoretical calculation confirm the better activity of Pt-NiFe LDH than NiFe LDH.

4. Conclusion

In summary, we reported a Pt-NiFe LDH as a superior OER and HER

electrocatalyst. Notably, the Pt-NiFe LDH has achieved remarkable overall water splitting performance, and the electrolyzer can maintain a current density of 1000 mA cm $^{-2}$ over 3000 h, which is a typical representative of high current density ultra-long stability water electrolytic catalyst compared with recent literature reports. *In-situ* optical microscopes suggests that gases are more likely to escape from the NF surface after electrochemical treatment. In addition, the DFT reveals that the introduction of Pt clusters on NiFe LDH reduces the energy barrier of OER. This work provides important fundamental insights for the development of highly active and stable electrocatalysts for water splitting.

CRediT authorship contribution statement

Xuedong He: Data curation, Investigation, Writing – original draft. **Xiang Han:** Data curation, Computation. **Xueyan Zhou:** Data curation, Investigation. **Jiadong Chen:** Computation, Writing – review & editing. **Juan Wang:** Supervision, Data curation, Investigation, Writing – review & editing. **Yan Chen:** Data curation. **Lianghao Yu:** Data curation. **Nan Zhang:** Writing – review & editing. **Shun Wang:** Funding acquisition.

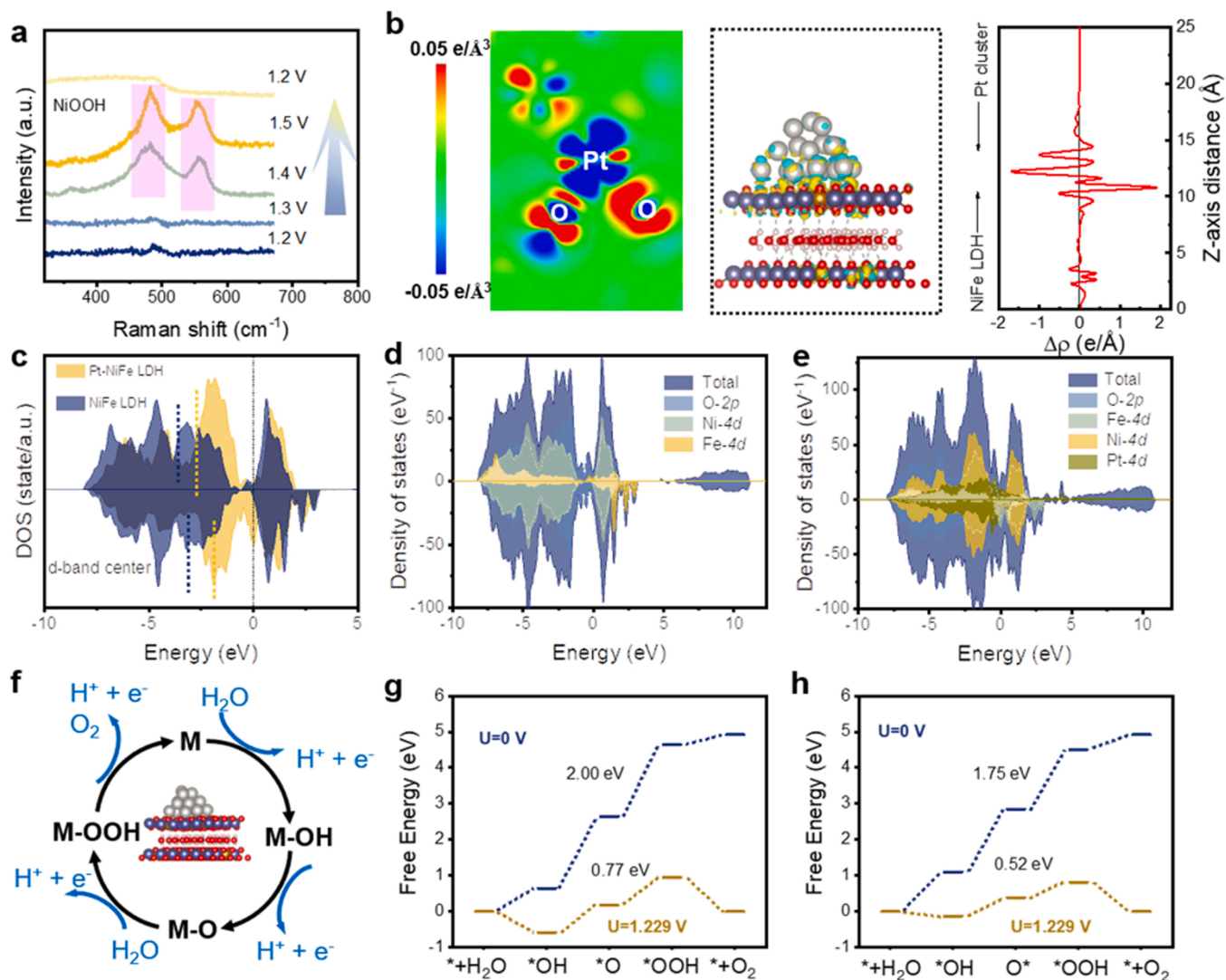


Fig. 5. (a) *In-situ* Raman spectra of Pt-NiFe LDH recorded from 1.2 to 1.5 V. (b) The 2D and 3D display of the differential charge density, and the corresponding planar averaged charge difference along the z-axis direction. Atoms are colored silver for Pt, red for O, pink for H, gold for Fe, and purple for Ni. (c) The projected DOS (pDOS) of the d states of Ni and Fe for NiFe LDH and Pt-NiFe LDH. The dotted line shows the d-band center. The Fermi level is set to zero. (d-e) The DOS of (d) NiFe LDH and (e) Pt-NiFe LDH. (f) Schematic illustration of the proposed OER mechanism. Gibbs free energy diagram for (g) NiFe LDH and (h) Pt-NiFe LDH.

Huile Jin: Supervision, Funding acquisition.

Declaration of Competing Interest

The authors declare that they have no known competing financial interests or personal relationships that could have appeared to influence the work reported in this paper.

Data Availability

No data was used for the research described in the article.

Acknowledgements

This work was supported by the National Natural Science Foundation of China (51872209 and 22105146) and Zhejiang Provincial Special Support Program for High-level Talents (2019R52042).

Appendix A. Supporting information

Supplementary data associated with this article can be found in the

online version at [doi:10.1016/j.apcatb.2023.122683](https://doi.org/10.1016/j.apcatb.2023.122683).

References

- [1] Y. Lei, Y. Wang, Y. Liu, C. Song, Q. Li, D. Wang, Y. Li, Designing atomic active centers for hydrogen evolution electrocatalysts, *Angew. Chem. Int. Ed.* 59 (2020) 20794–20812.
- [2] P. Wang, X. Zhang, J. Zhang, S. Wan, S. Guo, G. Lu, J. Yao, X. Huang, Precise tuning in platinum-nickel/nickel sulfide interface nanowires for synergistic hydrogen evolution catalysis, *Nat. Commun.* 8 (2017) 14580.
- [3] F. Dawood, M. Anda, G.M. Shafullah, Hydrogen production for energy: an overview, *Int. J. Hydrog. Energy* 45 (2020) 3847–3869.
- [4] Q. Wen, Y. Zhao, Y. Liu, H. Li, T. Zhai, Ultrahigh-current-density and long-term durability electrocatalysts for water splitting, *Small* 18 (2022), e2104513.
- [5] V.R. Stamenkovic, D. Strmcnik, P.P. Lopes, N.M. Markovic, Energy and fuels from electrochemical interfaces, *Nat. Mater.* 16 (2016) 57–69.
- [6] J. Wang, L. Han, B. Huang, Q. Shao, H.L. Xin, X. Huang, Amorphization activated ruthenium-tellurium nanorods for efficient water splitting, *Nat. Commun.* 10 (2019) 5692.
- [7] Y. Zhou, Y. Kuang, G. Hu, X. Wang, L. Feng, An effective Pt-CoTe/NC catalyst of bifunctional methanol electrolysis for hydrogen generation, *Mater. Today Phys.* 27 (2022), 100831.
- [8] T. Reier, M. Oezaslan, P. Strasser, Electrocatalytic oxygen evolution reaction (OER) on Ru, Ir, and Pt catalysts: a comparative study of nanoparticles and bulk materials, *ACS Catal.* 2 (2012) 1765–1772.

- [9] A. Bouzid, P. Gono, A. Pasquarello, Reaction pathway of oxygen evolution on Pt(1 1 1) revealed through constant Fermi level molecular dynamics, *J. Catal.* 375 (2019) 135–139.
- [10] S. Chandrasekaran, L. Yao, L. Deng, C. Bowen, Y. Zhang, S. Chen, Z. Lin, F. Peng, P. Zhang, Recent advances in metal sulfides: from controlled fabrication to electrocatalytic, photocatalytic and photoelectrochemical water splitting and beyond, *Chem. Soc. Rev.* 48 (2019) 4178–4280.
- [11] W. Song, M. Li, C. Wang, X. Lu, Electronic modulation and interface engineering of electrospun nanomaterials-based electrocatalysts toward water splitting, *Carbon Energy* 3 (2020) 101–128.
- [12] P. Liu, B. Chen, C. Liang, W. Yao, Y. Cui, S. Hu, P. Zou, H. Zhang, H.J. Fan, C. Yang, Tip-enhanced electric field: a new mechanism promoting mass transfer in oxygen evolution reactions, *Adv. Mater.* 33 (2021), e2007377.
- [13] Z. Sun, Y. Wang, L. Zhang, H. Wu, Y. Jin, Y. Li, Y. Shi, T. Zhu, H. Mao, J. Liu, C. Xiao, S. Ding, Simultaneously realizing rapid electron transfer and mass transport in Jellyfish-like Mott-Schottky nanoreactors for oxygen reduction reaction, *Adv. Funct. Mater.* 30 (2020), 1910482.
- [14] Y. Peng, H. Hajiyani, R. Pentcheva, Influence of Fe and Ni doping on the OER performance at the $\text{Co}_3\text{O}_4(001)$ surface: insights from DFT+U calculations, *ACS Catal.* 11 (2021) 5601–5603.
- [15] D.M. Morales, M.A. Kazakova, S. Dieckhöfer, A.G. Selyutin, G.V. Golubtsov, W. Schuhmann, J. Masa, Trimetallic Mn-Fe-Ni oxide nanoparticles supported on multi-walled carbon nanotubes as high-performance bifunctional ORR/OER electrocatalyst in alkaline media, *Adv. Funct. Mater.* 30 (2019), 1905992.
- [16] S.Y. Lee, I.S. Kim, H.S. Cho, C.H. Kim, Y.K. Lee, Resolving potential-dependent degradation of electrodeposited $\text{Ni}(\text{OH})_2$ catalysts in alkaline oxygen evolution reaction (OER): in situ XANES studies, *Appl. Catal., B* 284 (2021), 119729.
- [17] F. Bao, E. Kemppainen, I. Dorbandt, F. Xi, R. Bors, N. Maticic, R. Wenisch, R. Bagacki, C. Schary, U. Michalczyk, P. Bogdanoff, I. Lauermann, R. van de Krol, R. Schlattmann, S. Calnan, Host, suppressor, and promoter-the roles of Ni and Fe on oxygen evolution reaction activity and stability of NiFe alloy thin films in alkaline media, *ACS Catal.* 11 (2021) 10537–10552.
- [18] A. Saad, D. Liu, Y. Wu, Z. Song, Y. Li, T. Najam, K. Zong, P. Tsiakaras, X. Cai, Ag nanoparticles modified crumpled borophene supported Co_3O_4 catalyst showing superior oxygen evolution reaction (OER) performance, *Appl. Catal., B* 298 (2021), 120529.
- [19] J. Zhang, J. Liu, L. Xi, Y. Yu, N. Chen, S. Sun, W. Wang, K.M. Lange, B. Zhang, Single-atom Au/NiFe layered double hydroxide electrocatalyst: probing the origin of activity for oxygen evolution reaction, *J. Am. Chem. Soc.* 140 (2018) 3876–3879.
- [20] Z. Qiu, C.W. Tai, G.A. Niklasson, T. Edvinsson, Direct observation of active catalyst surface phases and the effect of dynamic self-optimization in NiFe-layered double hydroxides for alkaline water splitting, *Energy Environ. Sci.* 12 (2019) 572–581.
- [21] J. Wu, Z.F. Wang, T. Guan, G. Zhang, J. Zhang, J. Han, S. Guan, N. Wang, J. Wang, K. Li, Optimizing band structure of CoP nanoparticles via rich-defect carbon shell toward bifunctional electrocatalysts for overall water splitting, *Carbon Energy* (2022) <https://doi.org/10.1002/cey2.268>.
- [22] B. Lu, D. Wang, C. Zhao, K. Zhu, J. Yan, G. Wang, D. Cao, K. Ye, The novel dual-catalytic active sites of NiCoP/CoP as high-performance electrocatalyst for urea electrolysis and synergistic hydrogen production, *Mater. Chem. Front.* 6 (2022) 1681–1689.
- [23] H. Liu, X. Li, L. Chen, X. Zhu, P. Dong, M.O.L. Chee, M. Ye, Y. Guo, J. Shen, Monolithic Ni-Mo-B bifunctional electrode for large current water splitting, *Adv. Funct. Mater.* 32 (2021), 2107308.
- [24] P. Hou, D. Li, N. Yang, J. Wan, C. Zhang, X. Zhang, H. Jiang, Q. Zhang, L. Gu, D. Wang, Delicate control on the shell structure of hollow spheres enables tunable mass transport in water splitting, *Angew. Chem. Int. Ed.* 60 (2021) 6926–6931.
- [25] Y.F. Li, First-principles simulations for morphology and structural evolutions of catalysts in oxygen evolution reaction, *ChemSusChem* 12 (2019) 1846–1857.
- [26] L. Lv, Z. Yang, K. Chen, C. Wang, Y. Xiong, 2D layered double hydroxides for oxygen evolution reaction: from fundamental design to application, *Adv. Energy Mater.* 9 (2019), 1803358.
- [27] D. Yan, Y. Li, J. Huo, R. Chen, L. Dai, S. Wang, Defect chemistry of nonprecious-metal electrocatalysts for oxygen reactions, *Adv. Mater.* 29 (2017), 1606459.
- [28] N.K. Oh, J. Seo, S. Lee, H.J. Kim, U. Kim, J. Lee, Y.K. Han, H. Park, Highly efficient and robust noble-metal free bifunctional water electrolysis catalyst achieved via complementary charge transfer, *Nat. Commun.* 12 (2021) 4606.
- [29] L. Sha, T. Liu, K. Ye, K. Zhu, J. Yan, J. Yin, G. Wang, D. Cao, A heterogeneous interface on $\text{NiS@Ni}_3\text{S}_2/\text{NiMoO}_4$ heterostructures for efficient urea electrolysis, *J. Mater. Chem. A* 8 (2020) 18055–18063.
- [30] R. Ramesh, D.K. Nandi, T.H. Kim, T. Cheon, J. Oh, S.H. Kim, Atomic-layer-deposited MoNx thin films on three-dimensional Ni foam as efficient catalysts for the electrochemical hydrogen evolution reaction, *ACS Appl. Mater. Interfaces* 11 (2019) 17321–17332.
- [31] Y. Niu, Y. Yuan, Q. Zhang, F. Chang, L. Yang, Z. Chen, Z. Bai, Morphology-controlled synthesis of metal-organic frameworks derived lattice plane-altered iron oxide for efficient trifunctional electrocatalysts, *Nano Energy* 82 (2021), 105699.
- [32] C. Ouyang, L. Zheng, Q. Zhang, X. Wang, A simple preheating-pyrolysis strategy leading to superior oxygen reduction reaction activity in Fe-N/carbon black, *Adv. Mater.* 34 (2022), e2205372.
- [33] G. Kresse, J. Hafner, Ab initio molecular dynamics for liquid metals, *Phys. Rev. B Condens. Matter* 47 (1993) 558–561.
- [34] A. Notario-Estevéz, S.M. Kozlov, F. Vines, F. Illas, Electronic-structure-based material descriptors: (in)dependence on self-interaction and Hartree-Fock exchange, *Chem. Commun.* 51 (2015) 5602–5605.
- [35] P.E. Blochl, Projector augmented-wave method, *Phys. Rev. B Condens. Matter* 50 (1994) 17953–17979.
- [36] G. Kresse, D. Joubert, From ultrasoft pseudopotentials to the projector augmented-wave method, *Phys. Rev. B* 59 (1999) 1758–1775.
- [37] J.M.P. Martínez, E.A. Carter, Unraveling oxygen evolution on iron-doped beta-nickel oxyhydroxide: The key role of highly active molecular-like sites, *J. Am. Chem. Soc.* 141 (2019) 693–705.
- [38] Y. Hao, Y. Li, J. Wu, L. Meng, J. Wang, C. Jia, T. Liu, X. Yang, Z.P. Liu, M. Gong, Recognition of Surface Oxygen intermediates on NiFe oxyhydroxide oxygen-evolving catalysts by homogeneous oxidation reactivity, *J. Am. Chem. Soc.* 143 (2021) 1493–1502.
- [39] Y. Tian, X. Liu, L. Xu, D. Yuan, Y. Dou, J. Qiu, H. Li, J. Ma, Y. Wang, D. Su, S. Zhang, Engineering crystallinity and oxygen vacancies of $\text{Co}(\text{II})$ oxide nanosheets for high performance and robust rechargeable Zn-air batteries, *Adv. Funct. Mater.* 31 (2021), 2101239.
- [40] Y. Hu, G. Luo, L. Wang, X. Liu, Y. Qu, Y. Zhou, F. Zhou, Z. Li, Y. Li, T. Yao, C. Xiong, B. Yang, Z. Yu, Y. Wu, Single Ru atoms stabilized by hybrid amorphous/crystalline FeCoNi layered double hydroxide for ultraefficient oxygen evolution, *Adv. Energy Mater.* 11 (2020), 2002816.
- [41] T. Yao, N. Hou, J. Gan, J. Wang, X. Zhi, L. Fan, T. Gan, Y. Zhao, Y. Li, Enhanced activity and stability of $\text{Sr}_2\text{FeMo}_{0.65}\text{Ni}_{0.35}\text{O}_{6-\delta}$ anode for solid oxide fuel cells with Na doping, *J. Power Sources* 425 (2019) 103–109.
- [42] S. Alayoglu, A.U. Nilekar, M. Mavrikakis, B. Eichhorn, Ru-Pt core-shell nanoparticles for preferential oxidation of carbon monoxide in hydrogen, *Nat. Mater.* 7 (2008) 333–338.
- [43] B.M. Hunter, W. Hieringer, J.R. Winkler, H.B. Gray, A.M. Müller, Effect of interlayer anions on [NiFe]-LDH nanosheet water oxidation activity, *Energy Environ. Sci.* 9 (2016) 1734–1743.
- [44] K. Jiang, B. Liu, M. Luo, S. Ning, M. Peng, Y. Zhao, Y.R. Lu, T.S. Chan, F.M.F. de Groot, Y. Tan, Single platinum atoms embedded in nanoporous cobalt selenide as electrocatalyst for accelerating hydrogen evolution reaction, *Nat. Commun.* 10 (2019) 1743.
- [45] P. Zhai, M. Xia, Y. Wu, G. Zhang, J. Gao, B. Zhang, S. Cao, Y. Zhang, Z. Li, Z. Fan, C. Wang, X. Zhang, J.T. Miller, L. Sun, J. Hou, Engineering single-atomic ruthenium catalytic sites on defective nickel-iron layered double hydroxide for overall water splitting, *Nat. Commun.* 12 (2021) 4587.
- [46] C. Huang, Q. Zhou, D. Duan, L. Yu, W. Zhang, Z. Wang, J. Liu, B. Peng, P. An, J. Zhang, L. Li, J. Yu, Y. Yu, The rapid self-reconstruction of Fe-modified Ni hydroxysulfide for efficient and stable large-current-density water/seawater oxidation, *Energy Environ. Sci.* 15 (2022) 4647–4658.
- [47] S. Anantharaj, S. Kundu, S. Noda, The Fe effect: A review unveiling the critical roles of Fe in enhancing OER activity of Ni and Co based catalysts, *Nano Energy* 80 (2021), 105514.
- [48] H. Yan, Y. Xie, A. Wu, Z. Cai, L. Wang, C. Tian, X. Zhang, H. Fu, Anion-modulated HER and OER activities of 3D Ni-V-based interstitial compound heterojunctions for high-efficiency and stable overall water splitting, *Adv. Mater.* 31 (2019), e1901174.
- [49] Y.R. Zheng, P. Wu, M.R. Gao, X.L. Zhang, F.Y. Gao, H.X. Ju, R. Wu, Q. Gao, R. You, W.X. Huang, S.J. Liu, S.W. Hu, J. Zhu, Z. Li, S.H. Yu, Doping-induced structural phase transition in cobalt diselenide enables enhanced hydrogen evolution catalysis, *Nat. Commun.* 9 (2018) 2533.
- [50] D. Wang, Q. Li, C. Han, Q. Lu, Z. Xing, X. Yang, Atomic and electronic modulation of self-supported nickel-vanadium layered double hydroxide to accelerate water splitting kinetics, *Nat. Commun.* 10 (2019) 3899.
- [51] L. Liang, H. Jin, H. Zhou, B. Liu, C. Hu, D. Chen, Z. Wang, Z. Hu, Y. Zhao, H.W. Li, D. He, S. Mu, Cobalt single atom site isolated Pt nanoparticles for efficient ORR and HER in acid media, *Nano Energy* 88 (2021), 106221.
- [52] F. Zhang, Y. Shi, T. Xue, J. Zhang, Y. Liang, B. Zhang, In situ electrochemically converting $\text{Fe}_2\text{O}_3\text{-Ni}(\text{OH})_2$ to $\text{NiFe}_2\text{O}_4\text{-NiOOH}$: a highly efficient electrocatalyst towards water oxidation, *Sci. China Mater.* 60 (2017) 324–334.
- [53] Q. Wen, K. Yang, D. Huang, G. Cheng, X. Ai, Y. Liu, J. Fang, H. Li, L. Yu, T. Zhai, Schottky heterojunction nanosheet array achieving high-current-density oxygen evolution for industrial water splitting electrolyzers, *Adv. Energy Mater.* 11 (2021), 2102353.
- [54] A.R. Zeradjanian, P. Narangoda, I. Spanos, J. Masa, R. Schlögl, How to minimise destabilising effect of gas bubbles on water splitting electrocatalysts? *Curr. Opin. Electrochem.* 30 (2021), 100797.
- [55] Y. Tian, Z. Wu, M. Li, Q. Sun, H. Chen, D. Yuan, D. Deng, B. Johannessen, Y. Wang, Y. Zhong, L. Xu, J. Lu, S. Zhang, Atomic modulation and structure design of Fe-N_4 modified hollow carbon fibers with encapsulated Ni nanoparticles for rechargeable Zn-air batteries, *Adv. Funct. Mater.* 32 (2022), 2209273.
- [56] W. Peng, A. Deshmukh, N. Chen, Z. Lv, S. Zhao, J. Li, B. Yan, X. Gao, L. Shang, Y. Gong, L. Wu, M. Chen, T. Zhang, H. Gou, Deciphering the dynamic structure evolution of Fe- and Ni-codoped CoS_2 for enhanced water oxidation, *ACS Catal.* 12 (2022) 3743–3751.
- [57] X. Guo, X. Wan, Q. Liu, Y. Li, W. Li, J. Shui, Phosphated IrMo bimetallic cluster for efficient hydrogen evolution reaction, *eScience* 2 (2022) 304–310.